Title
Tunable quantum-cascade VECSEL operating at 1.9 THz.

Journal
Optics Express, 29(21)

ISSN
1094-4087

Authors
Wu, Yu
Shen, Yue
Addamane, Sadhvikas
et al.

Publication Date
2021-10-11

DOI
10.1364/oe.438636

Peer reviewed

Tunable quantum-cascade VECSEL operating at 1.9 THz

Yu Wu,[1] Yue Shen,[1] Sadhvikas Addamane,[2] John L. Reno,[2] and Benjamin S. Williams[1*]

[1]*Department of Electrical and Computer Engineering, University of California, Los Angeles, California 90095, USA*
[2]*Sandia National Laboratories, Center of Integrated Nanotechnologies, MS 1303, Albuquerque, New Mexico 87185, USA*
**bswilliams@ucla.edu*

Abstract: We report a terahertz quantum-cascade vertical-external-cavity surface-emitting laser (QC-VECSEL) emitting around 1.9 THz with up to 10% continuous fractional frequency tuning of a single laser mode. The device shows lasing operation in pulsed mode up to 102 K in a high-quality beam, with the maximum output power of 37 mW and slope efficiency of 295 mW/A at 77 K. Challenges for up-scaling the operating wavelength in QC metasurface VECSELs are identified.

1. Introduction:

Terahertz (THz) quantum-cascade (QC) lasers have so far been demonstrated as sources of radiation at frequencies between 1.2 THz and 5.6 THz [1–3], among which, high performance QC-lasers at frequencies below 2 THz are considered of particular interest. For example, THz QC-lasers at 1.9 THz have potential applications as local oscillators for large format heterodyne arrays in studying star formation processes. This is due to the fact that an important cooling mechanism of the diffuse interstellar medium occurs through emission at 1.90 THz from ionized carbon [CII] [4,5]. Another application involves QC-laser based terahertz imaging for non-destructive evaluation and security screening since at lower frequencies absorption and scattering of THz radiation tend to be reduced in many materials [6,7]. Furthermore, there are several atmospheric transmission windows between 1-2 THz [8]. Operation within those windows is not only advantageous for standoff imaging [9], but also for next generation wireless communication. Indeed, 6G protocols are beginning to be mapped out up to 3 THz [10,11].

However, designing THz QC-lasers below 2 THz is challenging. For example, the gain provided by the QC-active material suffers, as obtaining a population inversion between closely spaced subbands ($h\nu \approx 8$ meV at 2 THz) reduces the selectivity of injection and removal of electrons. This tends to reduce the dynamic range between the threshold current I_{th} and the maximum achievable current I_{max}, which in turn reduces the operating temperature and maximum output power [2,12–17]. Furthermore, for conventional metal-metal waveguide-based QC-lasers, output power and beam quality tend to suffer at lower frequencies, as the wavelength becomes longer ($\lambda \approx 150\ \mu$m at 2 THz), compared to the subwavelength dimension of the waveguide facets (typically 10 μm high) [18].

In this paper, we report a QC vertical-external-cavity surface-emitting laser (VESCEL) emitting at 1.9 THz. THz QC-VECSELs can achieve both high output power and high-quality beam patterns, as well as large fractional single-mode tuning [19,20]. The key component of a QC-VECSEL is an amplifying metasurface – a subwavelength reflectarray of metal-metal ridge waveguides loaded with QC-gain material. The amplifying metasurface is further paired with an output coupler to form the laser cavity. So far, QC-VECSELs have been demonstrated in the frequency range of 2.5-4.6 THz, with the best performance (i.e. highest powers and efficiencies)

in the 3-4 THz range [21–23]. In this demonstration, we have re-scaled the metasurface design to operate at a lower frequency, while preserving 10% continuous fractional frequency tuning of a single lasing mode by using intracryostat piezoelectric control of the cavity length.

2. Active region and metasurface design:

The metasurface is loaded with a GaAs/$Al_{0.15}Ga_{0.85}As$ QC-active region based upon the hybrid bound-to-continuum/resonant-phonon design scheme [24]; it is similar to that used in [20,25] except that the gain peak is scaled from 3.8 THz to 1.8 THz. See Appendix A for a band diagram at design bias. The layer sequence consists of alternating layers of $Al_{0.15}Ga_{0.85}As$/GaAs with the following thicknesses: 11.3/**2.1**/10.3/**3.7**/8.8/**4.0**/17.7/**5.4** nm, where the barrier layers are in bold and the central 5.9 nm of the underlined well is nominally Si-doped at 5×10^{16} cm^{-3}. It was grown by molecular beam epitaxy with 158 repeated modules for a total active region thickness of 10 μm (wafer number VA1032). Since this fabrication procedure yields a Schottky contact on the top of the heterostructure, applying reverse bias to an on-chip test mesa allows one to perform a conventional capacitance vs. voltage measurement to obtain the average doping concentration of the active region. We extract an average doping of 5.7×10^{15} cm^{-3}, which suggests carrier densities are ~20% higher than designed. To characterize the active material by itself, it was first fabricated into a 65 μm × 1510 μm edge-emitting metal-metal ridge waveguide device with dry-etched facets. It was tested in pulsed mode with 0.5% duty cycle (500 ns pulses at 10 kHz repetition rate) at various heat sink temperatures and its temperature performance was characterized and plotted in Figure 1(a-b). Emission spectrum shows lasing modes in the range from 1.95-2.12 THz; this range represents where the gain spectrum is maximum. While this is slightly higher in frequency than designed, as we will see below there is still significant gain at lower frequencies. Measurable output power above the noise floor was obtained up to 103 K (Fig. 1(b)) using a pyroelectric detector (GentecEO) placed adjacent to the cryostat window, however, the observation of a discontinuity in differential conductance (*dI/dV*) at threshold indicates continued lasing up to 117 K (Fig. 1(a), yellow curve). This maximum operating temperature is similar to that measured in other bound-to-continuum and resonant-phonon designs below 2 THz, but lower than that observed in scattering-assisted injection devices [12–15].

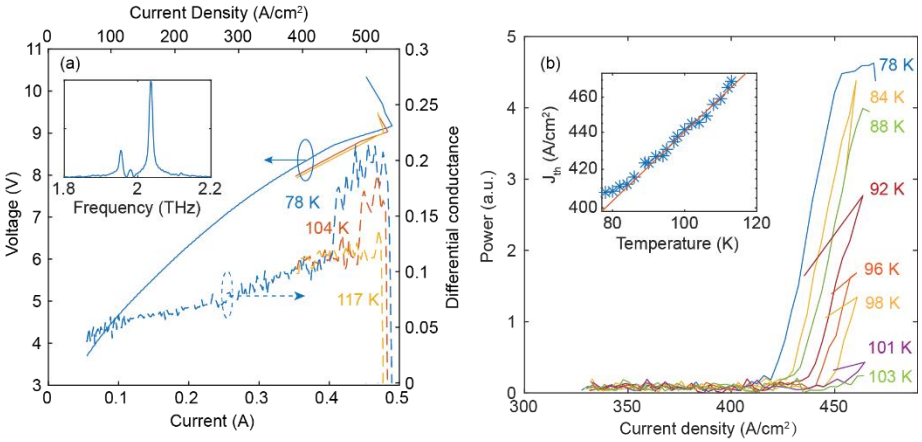

Fig. 1. (a) Pulsed-mode *dI/dV-I-V* characteristics measured at 78 K (blue), 104 K (red) and 117 K (yellow) of a 65 μm × 1510 μm edge-emitting metal-metal ridge waveguide device fabricated from QC-wafer VA1032. The inset plot shows a typical emission spectrum at 78 K measured using the Fourier-transform infrared (FTIR, Nicolet 8700) spectrometer with a resolution of 0.25 cm^{-1}. (b) The pulsed *P-I* characteristics as a function of varying heat-sink temperatures. The inset plot shows a phenomenological fit to the expression $J_{th}= J_0 \exp(T/T_0)$ with J_0= 291 A/cm², T_0 = 240 K.

In Fig. 1(b), a phenomenological fit to the expression $J_{th} = J_0 \exp(T/T_0)$ is plotted in the inset, which results in a value of J_0 = 291 A/cm^2 and T_0 = 240 K. The absolute power was unable

to be precisely measured in pulsed mode, as it was very low – as mentioned above, this is typical for the edge-emitting metal-metal waveguide geometry with a 10 μm high facet which exhibits low facet reflectivity and a highly divergent pattern leading to low collection efficiency.

The QC-active material was then fabricated into a metasurface with an array of metal-metal ridge antennas (Fig. 2(a)). The ridge width and period are measured via scanning electron microscopy to be $w = 20.9$ μm and $\Lambda = 75$ μm, which sets the metasurface resonance at 1.92 THz. Although slightly lower than the frequency of peak gain of the QC-active material, it is very close to the aforementioned [CII] line at 1.90 THz. These dimensions are approximately linearly scaled from a 3.5 THz metasurface reported in [20]. The metasurface is spatially uniform across the 3 × 3 mm^2 area, although a patterned oxide layer underneath the top metallization allows electrical bias to be selectively applied to a central circular area of diameter 1.5 mm. This preferentially pumps the fundamental Gaussian mode within the cavity. Microfabrication of the QC metasurface takes place in the standard metal-metal waveguide process using a Cu-Cu thermocompression wafer bonding technique [26]. Experimental confirmation of the design was provided by THz time domain spectroscopy (TDS), which was used to directly measure the passive reflectance and reflection phase spectra at normal incidence at room temperature [27,28]. The experimental reflectance characteristics are plotted in Fig. 2(b) in blue and is compared with the full-wave 2D finite-element (FEM) electromagnetic reflectance simulation results using COMSOL Multiphysics (red and yellow dashed curves). In FEM simulation, the metasurface is assumed to be infinite in extent, where a single metasurface period is simulated with periodic boundary conditions. Simulated losses in the metal thin films are estimated using the Drude model (n_{Au} = 5.9 × 10^{22} cm^{-3}, $\tau_{Au,300\ K}$ = 18.6 fs, $\tau_{Au,77\ K}$ = 39 fs [29]), while for the semiconductor layer, the band diagram simulated at zero bias indicates that there exists strong absorption loss coming from a ~1.9 THz intersubband resonance within the active material [28]. Modeling details of this intersubband absorption loss is included in Appendix A. The simulated spectra at room temperature indicate a metasurface resonant frequency well matched with experimental results. Though the reflectance dip is not as deep as that observed in TDS experiment, it suggests that the metasurface is very strongly absorbing in the unbiased regions; furthermore, it likely becomes more lossy at 77 K as the intersubband population difference is expected to increase. As we will see below this has consequences for the cavity design.

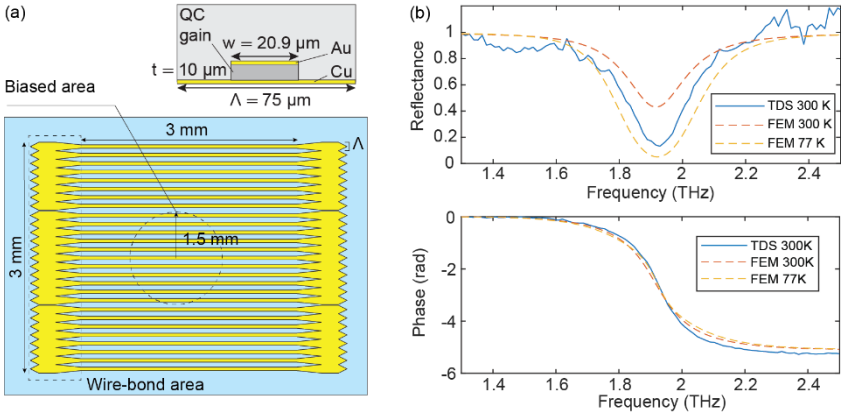

Fig. 2. (a) Top-down schematic of active QC-metasurface designed at 1.9 THz. (b) Passive reflectance and phase spectra measured using reflection-mode TDS at room temperature (blue curves), and FEM simulated spectra at 300 K (red dashed curves) and at 77 K (yellow dashed curves).

3. Results:

The VECSEL cavity was constructed by pairing the QC-metasurface with planar inductive-mesh output couplers (OCs) of the type that has been used in previous QC-VECSEL

experiments [30]. In the experiments, the device was tested with both a relatively less reflective output coupler (labeled OC1, transmittance ~4-8%) and a more reflective output coupler (labeled OC2, transmittance ~2-6%), both with the same quartz substrate but different metallic meshes. Details of the output couplers are given in Appendix B. The output coupler was mounted inside the cryostat on a single axis piezoelectric stepping stage (Attocube ANPx311) that can be used to adjust the cavity length (and correspondingly the lasing frequency). All measurements were performed at 77 K in pulsed mode with 0.5% duty cycle (500 ns pulses at 10 kHz repetition rate).

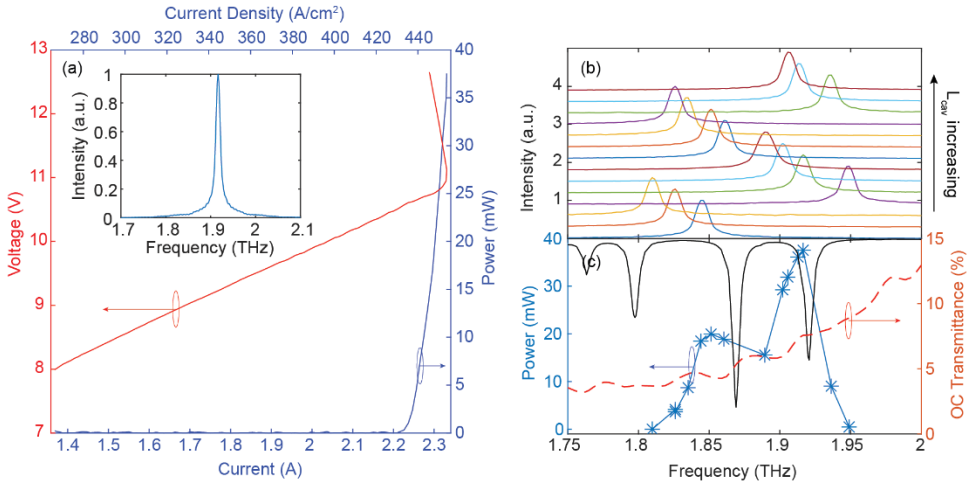

Fig. 3. (a) Pulsed-mode *P-I-V* characteristics of the QC-VECSEL using a relative low reflectance output coupler (OC1). Inset shows the corresponding FTIR spectrum at 1.92 THz. (b) Single-mode lasing spectra measured as the piezoelectric stage was stepped, tuning the external cavity length. (c) The variation of output power as a function of lasing frequency (blue). Experimental transmittance of OC1 is ~4-8% around 1.9 THz indicated by the red dashed line. The black curve indicates the atmospheric transmission features within the lasing frequency tuning range.

Results using the less reflective mesh output coupler OC1 are plotted in Figures 3-5. The THz power and voltage vs. current (*P-I-V*) curves are plotted in Fig. 3(a), where the power was collected with a pyroelectric detector (GentecEO), and the absolute power levels were measured using a calibrated thermopile. A maximum output power of 37 mW is obtained at an optimized cavity length (after correction by the 75% transmittance through the 3 mm thick polyethylene cryostat window). A linear slope efficiency (dP/dI) of 295 mW/A is measured, which corresponds to 0.23 emitted photons per injected electron per module. The corresponding lasing spectrum at 1.92 THz was measured using the FTIR (Nicolet 8700) spectrometer with a resolution of 0.25 cm^{-1}. By stepping the piezoelectric stage, continuous tuning of single lasing mode was observed between 1.81 THz and 1.95 THz (Fig. 3(b)). This 140 GHz tuning range is limited by the free-spectral range (FSR) of the external cavity and an estimated cavity length around 1.1 mm is indicated from the FSR. *P-I-V* curves were collected at each lasing frequency and the measured output power is plotted in Fig. 3(c) along with the experimental output coupler transmittance (red dashed curve) and atmospheric transmission features calculated from the HITRAN database (black). The variation of output power is primarily a result of the changing output coupler transmittance as well as the frequency-dependent metasurface active reflectance. The fact that the maximum output power is observed at 1.92 THz is consistent with our measurement of the metasurface resonant frequency shown in Fig. 2(b). As the cavity is made shorter, lasing ceases as due to the combined effect of the reduced output coupler and metasurface reflectance to increase the required lasing threshold. A reduction of power was

observed for lasing modes around 1.87 THz, resulting from the existence of a strong water vapor absorption line.

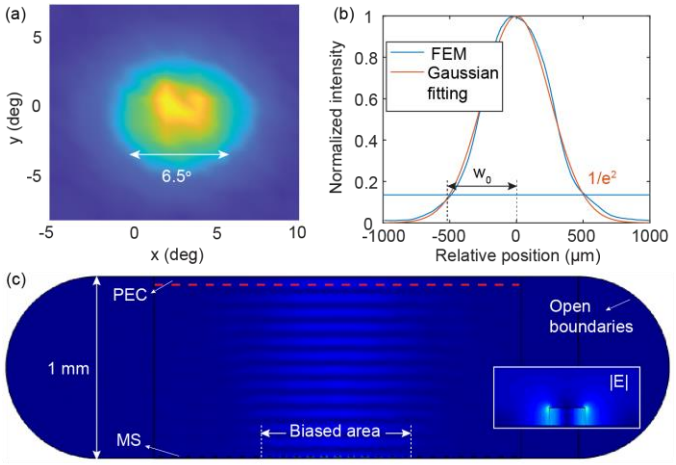

Fig. 4. (a) Far field beam pattern measured at the corresponding frequency of 1.92 THz using a relative low reflectance output coupler (OC1). (b) 1D intensity distribution along the red dashed line in (c) (blue) and its Gaussian fitting (red), which indicates an estimated beam waist of 505 μm. (c) 2D electric field plot of the FEM simulated cavity. The inset shows the E field distribution in a single ridge antenna.

The far-field beam pattern was measured at the lasing frequency of 1.92 THz using a 2-axis scanning pyroelectric detector (Fig. 4(a)), which indicated a circular, directive beam spot with a full-width half-maximum (FWHM) divergence angle of ~6.5°. To better understand the nature of the cavity mode and emitting beam, we constructed a 2D full-wave electromagnetic external cavity model using COMSOL Multiphysics, which accounts for the finite dimension of the metasurface along one axis. The output coupler is modeled as a perfect electric conductor (PEC) boundary, to form an external cavity around 1 mm long. The metasurface is 3 mm wide, however we assume that only the ridge antennas within a central length of 1.5 mm are selectively biased and loaded with uniform QC-gain. The ridge antennas outside of the central biased area are assumed be loaded with intersubband absorption loss (see Appendix A), and the metal losses are estimated using the Drude model – in agreement with the reflectance simulation

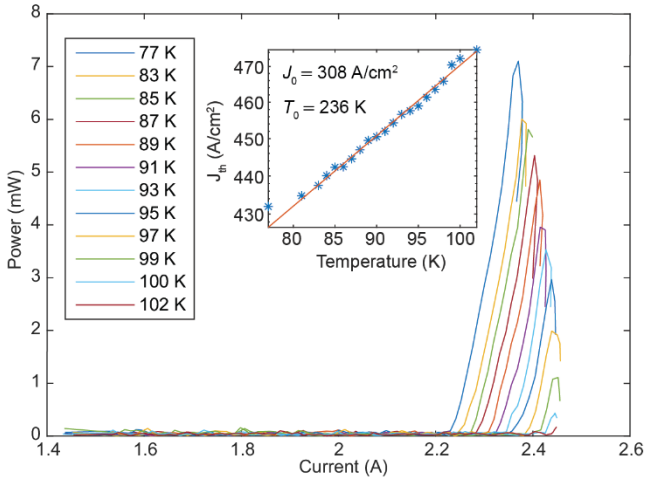

Fig. 5. The pulsed *P-I* characteristics of QC-VECSEL using OC1 as a function of the heat-sink temperature *T*. Inset shows a phenomenological fit to the expression $J_{th} = J_0 \exp(T/T_0)$ with $J_0 = 308$ A/cm^2, $T_0 = 236$ K.

discussed in Fig. 2(b) (yellow dashed lines). The QC-gain coefficient is chosen so that the cavity eigenfrequency is fully real (i.e. no net loss). 1D (along the red dashed line in Fig. 4(c)) and 2D field plots of the FEM simulated cavity are displayed in Fig. 4(b-c). An estimated intracavity beam radius of $w_0 = 505\ \mu$m is indicated in Fig. 4(b), defined as the position where the intensity has dropped to $1/e^2$ of its on-axis value. By approximating this intracavity mode as a fundamental Gaussian beam, and using the well-known relation for the $1/e^2$ full-width divergence angle $\Theta = 2\lambda/\pi w_0$, we obtain $\Theta \approx 11.3°$, which is equivalent to a full-width half-max divergence of 6.6°. This is in good agreement with the measured FWHM value in Fig. 4(a). This confirms that it is critical to consider the strong metasurface absorption that occurs in the unbiased regions of the metasurface, since this causes the cavity eigenmode to "self-localize" mostly to the biased region to minimize losses and maximize the modal confinement factor.

Fig. 5 shows the temperature performance of this QC-VECSEL device using OC1, where pulsed *P-I* characteristics as a function of varying heat-sink temperatures (T) demonstrate that the device lased up to a maximum temperature of 102 K. A phenomenological fit to the expression $J_{th} = J_0 \exp(T/T_0)$ is indicated in the inset, which results in values of $J_0 = 308$ A/cm^2, $T_0 = 236$ K. The T_0 value is essentially the same as for the metal-metal ridge waveguide within measurement uncertainty (Fig. 1(b)), which indicates that almost no additional thermal degradation is introduced due to the VECSEL configuration. The J_0 value is slightly higher which can be explained by the increased lasing threshold for VECSELs due to additional losses coming from the output coupler and light diffraction.

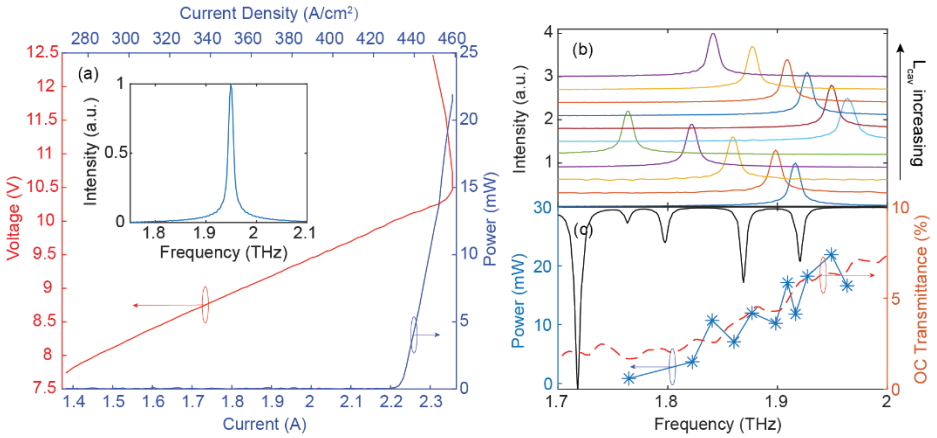

Fig. 6. (a) Pulsed-mode *P-I-V* characteristics of the QC-VECSEL using a relative high reflectance output coupler (OC2). Inset shows the FTIR spectrum at 1.95 THz. (b) Single-mode lasing spectra measured as the piezoelectric stage was stepped, tuning the external cavity length. (c) The variation of output power as a function of lasing frequency (blue). Experimental transmittance of OC2 is ~2-6% around 1.9 THz indicated by the red dashed line. The black curve indicates the atmospheric transmission features within the lasing frequency tuning range.

Results using a different, more reflective mesh output coupler (OC2) are plotted in Figure 6. Although the threshold current density is slightly reduced compared with OC1, the maximum power and slope efficiency drop. This can be explained by the reduced output coupler transmission; this reduces the beneficial out-coupling loss compared to diffractive and absorptive losses within the external cavity. Still, the reduced threshold helps to increase the tuning range (see Fig. 6(b-c)). By making the cavity length shorter (~0.75 mm), up to 200 GHz of continuous, single-mode frequency tuning was observed from 1.76 THz to 1.96 THz (10.7% fractional tuning). Again, the output power generally increases with lasing frequency due to the increase of output coupler transmittance in this frequency range, with the maximum power measured at a lasing frequency of 1.95 THz, slightly higher than that of OC1 (1.92 THz).

As a summary, we provide a table comparing the performance of three devices fabricated from the same QC-active region (VA1032): metal-metal ridge waveguide, QC-VECSEL using OC1, QC-VECSEL using OC2.

Table 1. Performance of metal-metal ridge waveguide, QC-VECSEL using OC1 and QC-VECSEL using OC2.

Device	T_{OC}	J_{th}	P_{max}	dP/dI	T_{max}	Tuning range
Metal-metal waveguide	N/A	419 A/cm^2	/	/	117 K	not tunable, multimode
QC-VECSEL (OC1)	~4-8%	430 A/cm^2	37 mW @1.92 THz	295 mW/A @ 1.92 THz	102 K	1.81 - 1.95 THz single mode
QC-VECSEL (OC2)	~2-6%	427 A/cm^2	22 mW @ 1.95 THz	148 mW/A @ 1.95 THz	/	1.76 - 1.96 THz single mode

4. Conclusion:

A QC-VECSEL is presented that operates at frequencies below 2 THz. This provides immediate advantages: the output power and slope efficiency are much higher compared with similar QC-lasers based on edge-emitting waveguides [13,17,31], at the same time allowing a high-quality beam and significant (10% fractional) single-mode tuning. The threshold current density and maximum pulsed operating temperature are only slightly degraded from the ridge waveguide case – T_{max} is comparable with some early works using similar resonant-tunneling injection scheme [12,14]. However, this demonstration is also illustrative of particular challenges for low-frequency QC-VECSELs. For example, while we measure slope efficiencies (~0.2 photons/electron/module) that are not too much smaller compared with good VECSELs in the > 3 THz range, the total powers are considerably lower due to the reduced dynamic range for current injection between J_{max} and J_{th}. As a result, the pulsed wall plug efficiency is on the order of 10^{-3}, about 10 times smaller than what has been reported for VECSELs at > 3 THz [22]. This is fundamentally related to the underlying active region; for such small separations between the radiative subbands ($h\nu \approx 8$ meV), it becomes difficult to selectively inject electrons into the upper state, without also injecting into the lower state. The presence of a strong sub-threshold parasitic leakage channel sets a floor under J_{th}, which means that even a slight increase in J_{th} associated with the extra VECSEL losses takes a big bite out of the output power.

Using the relationships described in Appendix C, we see that scaling the operating wavelength by a factor of S tends to reduce the available gain bandwidth for single-mode tuning. For example, if we keep both the metasurface fill factor $F=w/\Lambda$ and QC-active material height h constant, the radiative quality factor of the metasurface resonance scales up with a factor of S, such that the fractional tuning range scales down by a factor of S. This is roughly consistent with the 10% fractional tuning range observed here, compared with 19% observed at 3.5 THz in [20]. This trend can be counteracted if either the fill factor F is increased, or height h is increased, however both strategies will increase the metasurface power dissipation density which will impede continuous-wave (cw) operation. Furthermore, wavelength scaling also introduces challenges to maintain a low-loss cavity mode. In order to keep diffraction loss constant and prevent modal overlap with the lossy unbiased region, the bias area must be also up-scaled by S. Since the current density needed by the active region does not scale with wavelength, the device then draws more current which again impedes cw operation.

These results suggest several research directions for QC-VECSELs below 2 THz. First will be to improve the underlying QC-active region design for low frequency QC-lasers. For example, by using a scattering-assisted injection scheme, both the maximum operation temperature as well as the current dynamic range has been significantly improved in ~2 THz QC-lasers (163 K in [13], 160 K in [15], 144 K in [31]), although these designs tend to exhibit

a large voltage drop and high current density. Second, in order to enable continuous-wave operation, the metasurface power dissipation density can be reduced, for example by using a patch-antenna based metasurface [23], although this will come at the expense of a higher Q_r and reduced tuning bandwidth. Third, metasurface design to reduce the absorption from the unbiased metasurface region will reduce the loss penalty for the diffractive increase in modal size at low frequencies. In this way, one could potentially provide high-efficiency, cw, tunable THz QC-laser sources < 2 THz for imaging, spectroscopy, and heterodyne local oscillator applications.

Appendix A: Intersubband absorption loss

The reflection spectra of the passive metasurface measured at room temperature using THz TDS indicates that the absorption dip at the resonant frequency is much deeper than expected. For better explanation of the high semiconductor losses, we simulated the band diagram at zero bias using a self-consistent Schrödinger-Poisson solver, populated the subbands according to the Fermi-Dirac distribution, and identified the dominant intersubband transitions that would cause loss (Fig. 7). The dominant intersubband transition occurs between the subbands 2 and 3 at a frequency very close to the metasurface resonance (E_3-$E_2 = 8$ meV) with calculated oscillator strength of $f_{23} = 0.59$ – this can be expected to introduce strong absorption loss [28].

A Lorentz oscillator model is applied to model the effect of this intersubband transition on the z-component of the permittivity:

$$\varepsilon_z(\omega) = \varepsilon_{core} + \frac{(N_2 - N_3)e^2 f_{23}}{m^* L_{mod}} \frac{1}{\omega_{23}^2 - \omega^2 - i\omega\gamma}, \quad (1)$$

where $\varepsilon_{\text{core}}$ is the semiconductor permittivity excluding free carrier contributions, m^* is the GaAs electron effective mass, L_{mod} is the length of one module of the active region. We assume the averaged doping concentration of 5.7×10^{15} cm^{-3} is distributed throughout the lowest five subbands, which are populated according to a Fermi-Dirac distribution. Different 2D population differences $N_2 - N_3$ are calculated at room temperature and at 77 K according to the method described in [32]. An estimate value for the damping term γ is obtained from separately performed Nonequilibrium Green's functions (NEGF) simulations, and is set as $2\pi \times 750$ GHz at room temperature and $2\pi \times 410$ GHz at 77 K. As plotted in Fig. 2(b), the intersubband absorption loss is stronger at 77 K compared with that at room temperature due to larger population difference and smaller damping.

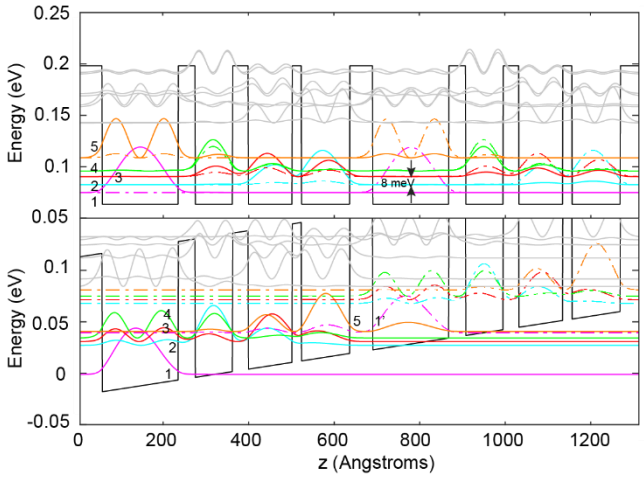

Fig. 7. Conduction band diagram of the active region at zero bias (upper) and at design bias (lower).

Appendix B: Output couplers

The OC comprises an inductive Ti/Au mesh evaporated on a nominally 100-μm-thick double-side-polished z-cut quartz substrate. The width and period of the mesh determine the overall transmittance magnitude. The transmittance of both output couplers used in this paper was experimentally measured using FTIR spectroscopy and is plotted in Fig. 8; it represents an expanded set of data shown in Figs. 3(c) and 6(c). The corresponding dimensions of the inductive mesh are shown in the insets of Fig. 8. The oscillations in the transmittance are related to standing wave interference within the quartz substrate.

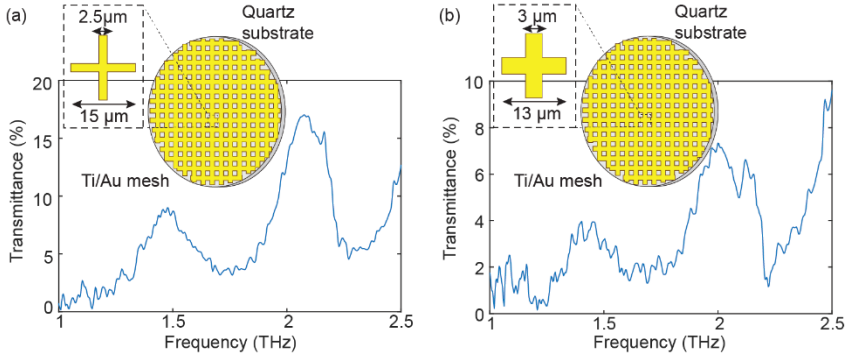

Fig. 8. Measured transmittance of metal-mesh output couplers OC1 (a) and OC2 (b). The dimensions of the inductive metallization are shown in the insets.

Appendix C: Wavelength scaling of QC-VECSELs

We present here approximate scaling relationships relevant for scaling of the metasurface resonant wavelength by a factor of S, such that $\lambda_0 \rightarrow S\lambda_0$, or equivalently the metasurface resonant frequency $\nu_0 \rightarrow \nu_0/S$. Assuming a weak-coupling approximation for metasurface interaction (i.e. the metasurface is far from perfect absorption when unbiased and far from the self-lasing condition when fully biased), we can write the approximate metasurface reflectance as:

$$R = e^{\xi(\nu)(g(\nu)-g_{tr})}, \tag{2}$$

where $\xi(\nu)$ is an effective interaction length with the QC-gain material and contains the lineshape information of the metasurface, and $g(\nu)$ is the QC material gain coefficient per unit length (in units of cm^{-1}) which contains the intersubband lineshape information of the material [33]. The transparency gain is written as g_{tr}, which includes all material losses of the QC material and the metasurface. As described in [33], by assuming a (albeit non-physical) frequency independent gain $g(\nu) = g$, simulating the reflectance of a given metasurface in a FEM solver allows us to numerically calculate $R(g)$, and extract $\xi(\nu)$ and g_{tr} as fitting parameters. However, as derived in [23], we can also use an analytic approximation for the peak interaction length:

$$\xi(\nu_0) = \frac{2\Gamma c Q_r}{\pi n \nu_0} = \frac{2\Gamma \lambda_0 Q_r}{\pi n}, \tag{3}$$

where Q_r is the radiative quality factor of the metasurface, n is the refractive index of the QC-active material, and Γ is a dimensionless near-field confinement factor which is usually slightly less than unity. Since both Q_r and $\xi(\nu_0)$ can be fit from the FEM simulations, Γ can be used as a fitting parameter. Finally, by using the cavity antenna model given in [34,35], we can derive an approximate expression for Q_r. If we consider a ridge antenna based metasurface, with ridges of width w, height h and subwavelength period of Λ (i.e. $\Lambda < 0.8\lambda_0$).

$$Q_r = \frac{n^2 w \pi \Lambda}{4 h \lambda_0}. \quad (4)$$

For a TM_{01} ridge metasurface, to first order the width of the ridge is determined by the half-wavelength resonance condition such as $w \approx \lambda_0/2n$. Using that approximation, we can write $Q_r = n\pi\Lambda/4h$. It is important to note that $Q_r \propto h^{-1}$; this is because the lateral sidewalls of the ridge antennas act as aperture antennas in the short dipole limit.

With these relationships, we now consider scaling the wavelength according to $\lambda_0 \rightarrow S\lambda_0$. We choose to keep the fill factor $F = w/\Lambda$ constant to keep the power dissipation density constant. We also choose to keep the height h constant since it is primarily determined by the number of QC periods grown. Under these conditions it implies that both the period and the width increase ($\Lambda \rightarrow S\Lambda$, $w \rightarrow Sw$). As a result, the radiative quality factor scales as $Q_r \rightarrow SQ_r$, and the interaction length scales as $\xi \rightarrow S^2\xi$. The increase in ξ can be interpreted as an increase in field enhancement and helps to mitigate the reduced material gain available at the frequency < 2 THz. However, the available maximum tuning range $\Delta\nu$ suffers ($\Delta\nu \rightarrow \Delta\nu/S^2$), since it is primarily limited by Q_r (assuming the underlying QC-media has sufficiently broadband available gain). This limitation can be eased if one is willing to scale up the ridge height h. However, this approach is somewhat undesirable, since it would impose a burden both on MBE growth time and uniformity, and it would result in a proportionally larger bias voltage. Furthermore, since the low thermal conductivity of the QC heterostructures serves as the thermal bottleneck to heat removal, a thicker active region would come at the detriment of cw operation.

Disclosures

Acknowledgements. We thank Mohammad Shahili for performing the capacitance vs. voltage measurements of carrier concentration and NEGF simulations. Microfabrication was performed at the UCLA Nanoelectronics Research Facility and wire bonding was performed at the UCLA Center for High Frequency Electronics. This work was performed, in part, at the Center for Integrated Nanotechnologies, an Office of Science User Facility operated for the U.S. Department of Energy (DOE) Office of Science. Sandia National Laboratories is a multimission laboratory managed and operated by National Technology and Engineering Solution of Sandia, LLC., a wholly owned subsidiary of Honeywell International, Inc., for the U.S. Department of Energy's National Nuclear Security Administration under contract DE-NA-0003525.

Funding. National Science Foundation (1711892, 1810163), National Aeronautics and Space Administration (80NSSC19K0700).

Data Availability. The data that supports the findings of this study are available within the article.

Disclosures. The authors declare no conflicts of interest.

References and links:

1. R. Kohler, A. Tredicucci, F. Beltram, H. E. Beere, E. H. Linfield, A. G. Davies, D. A. Ritchie, R. C. Iotti, and F. Rossi, "Terahertz semiconductor-heterostructure laser," Nature **417**(6885), 156–159 (2002).
2. C. Walther, M. Fischer, G. Scalari, R. Terazzi, N. Hoyler, and J. Faist, "Quantum cascade lasers operating from 1.2 to 1.6 THz," Appl. Phys. Lett. **91**(13), 1–4 (2007).
3. L. Li, I. Kundu, P. Dean, E. H. Linfield, and A. G. Davies, "High-power GaAs / AlGaAs quantum cascade lasers with," (September), 7–9 (2016).
4. C. Walker, C. Kulesa, J. Kloosterman, D. Lesser, T. Cottam, C. Groppi, J. Zmuidzinas, M. Edgar, S. Radford, P. Goldsmith, W. Langer, H. Yorke, J. Kawamura, I. Mehdi, D. Hollenbach, J. Stutzki, H. Huebers, J. R. Gao, and C. Martin, "Large format heterodyne arrays for observing far-infrared lines with SOFIA," Millimeter, Submillimeter, Far-Infrared Detect. Instrum. Astron. V **7741**, 77410Z (2010).
5. W. D. Langer, T. Velusamy, J. L. Pineda, P. F. Goldsmith, D. Li, and H. W. Yorke, "C+ detection of warm dark gas in diffuse clouds," Astron. Astrophys. **521**(1), 4–7 (2010).
6. W. R. Tribe, D. A. Newnham, P. F. Taday, and M. C. Kemp, "Hidden object detection: security applications of terahertz technology," Terahertz Gigahertz Electron. Photonics III **5354**, 168–176 (2004).
7. Y. C. Shen, T. Lo, P. F. Taday, B. E. Cole, W. R. Tribe, and M. C. Kemp, "Detection and identification of explosives using terahertz pulsed spectroscopic imaging," Appl. Phys. Lett. **86**(24), 1–3 (2005).
8. Y. Yang, A. Shutler, and D. Grischkowsky, "Measurement of the transmission of the atmosphere from 0.2 to 2 THz," Opt. InfoBase Conf. Pap. **19**(9), 8830–8838 (2011).
9. A. W. M. Lee, Q. Qin, S. Kumar, B. S. Williams, Q. Hu, and J. L. Reno, "Real-time terahertz imaging over a standoff distance (>25 meters)," Appl. Phys. Lett. **89**(14), 2–5 (2006).
10. NTT DOCOMO, INC. "White paper: 5G Evolution and 6G," (2020). https://www.nttdocomo.co.jp/english/binary/pdf/corporate/technology/whitepaper_6g/DOCOMO_6G_White_PaperEN_20200124.pdf
11. "FCC Opens Spectrum Horizons for New Services & Technologies," (Federal Communications Commission, 2019). https://docs.fcc.gov/public/attachments/DOC-356588A1.pdf
12. C. Walther, G. Scalari, J. Faist, H. Beere, and D. Ritchie, "Low frequency terahertz quantum cascade laser operating from 1.6 to 1.8 THz," Appl. Phys. Lett. **89**(23), 8–11 (2006).
13. S. Kumar, C. W. I. Chan, Q. Hu, and J. L. Reno, "A 1.8-THz quantum cascade laser operating significantly above the temperature of $\hbar\omega/k_B$," Nat. Phys. **7**(2), 166–171 (2011).
14. S. Kumar, B. S. Williams, Q. Hu, and J. L. Reno, "1.9 THz quantum-cascade lasers with one-well injector," Appl. Phys. Lett. **88**(12), 12–14 (2006).
15. S. Miho, T. T. Lin, and H. Hirayama, "1.9 THz selective injection design quantum cascade laser operating at extreme higher temperature above the kBT line," Phys. Status Solidi Curr. Top. Solid State Phys. **10**(11), 1448–1451 (2013).
16. G. Scalari, C. Walther, M. Fischer, R. Terazzi, H. Beere, D. Ritchie, and J. Faist, "THz and sub-THz quantum cascade lasers," Laser Photonics Rev. **3**(1–2), 45–66 (2009).
17. C. Worrall, J. Alton, M. Houghton, S. Barbieri, H. E. Beere, D. Ritchie, and C. Sirtori, "Continuous wave operation of a superlattice quantum cascade laser emitting at 2 THz," Opt. Express **14**(1), 171–181 (2006).
18. C. Wu, S. Khanal, J. L. Reno, and S. Kumar, "Terahertz plasmonic laser radiating in an ultra-narrow beam," Optica **3**, 734–740 (2016).
19. L. Xu, C. A. Curwen, P. W. C. Hon, Q. S. Chen, T. Itoh, and B. S. Williams, "Metasurface external cavity laser," Appl. Phys. Lett. **107**, 221105 (2015).
20. C. A. Curwen, J. L. Reno, and B. S. Williams, "Broadband continuous single-mode tuning of a short-cavity quantum-cascade VECSEL," Nat. Photonics **13**(12), 855–859 (2019).
21. L. Xu, C. A. Curwen, P. W. C. Hon, T. Itoh, and B. S. Williams, "Terahertz quantum cascade VECSEL," Proc. SPIE 9734, Vertical External Cavity Surface Emitting Lasers (VECSELs) VI, 97340G (2016)
22. C. A. Curwen, J. L. Reno, and B. S. Williams, "Terahertz quantum cascade VECSEL with watt-level output power," Appl. Phys. Lett. **113**, 011104 (2018).
23. C. A. Curwen, J. L. Reno, and B. S. Williams, "Terahertz quantum-cascade patch-antenna VECSEL with low power dissipation," Appl. Phys. Lett. **116**, 241103 (2020).
24. M. I. Amanti, G. Scalari, R. Terazzi, M. Fischer, M. Beck, J. Faist, A. Rudra, P. Gallo, and E. Kapon, "Bound-to-continuum terahertz quantum cascade laser with a single-quantum-well phonon extraction/injection stage," New J. Phys. **11**, 125022 (2009).
25. C. A. Curwen, J. L. Reno, and B. S. Williams, "Broadband metasurface design for terahertz quantum-cascade VECSEL," Electron. Lett. **56**(23), 1264–1267 (2020).
26. B. S. Williams, S. Kumar, Q. Hu, and J. L. Reno, "Operation of terahertz quantum-cascade lasers at 164 K in pulsed mode and at 117 K in continuous-wave mode," Opt. Express **13**(9), 3331–3339 (2005).
27. Y. Shen, A. D. Kim, C. A. Curwen, J. L. Reno, and B. S. Williams, "THz Time-Domain Characterization of Amplifying Quantum-Cascade Metasurface," Int. Conf. Infrared, Millimeter, Terahertz Waves, IRMMW-THz (2020).
28. Y. Shen, A. D. Kim, M. Shahili, S. Addamane, J. L. Reno, and B. S. Williams, "THz time-domain characterization of amplifying quantum-cascade metasurface" (manuscript in preparation).
29. N. Laman and D. Grischkowsky, "Terahertz conductivity of thin metal films," Appl. Phys. Lett. **93**(5), 1–4

(2008).
30. L. Xu, C. A. Curwen, J. L. Reno, and B. S. Williams, "High performance terahertz metasurface quantum-cascade VECSEL with an intra-cryostat cavity," Appl. Phys. Lett. **111**, 101101 (2017).
31. S. Khanal, J. L. Reno, and S. Kumar, "2.1 THz quantum-cascade laser operating up to 144 K based on a scattering-assisted injection design," Opt. Express **23**(15), 19689–19697 (2015).
32. C. Jirauschek and T. Kubis, "Modeling techniques for quantum cascade lasers," Appl. Phys. Rev. **1**, 011307 (2014).
33. L. Xu, C. A. Curwen, D. Chen, J. L. Reno, T. Itoh, and B. S. Williams, "Terahertz metasurface quantum-cascade VECSELs: Theory and performance," IEEE J. Sel. Top. Quantum Electron. **23**(6), 1200512 (2017).
34. P. W. C. Hon, Z. Liu, T. Itoh, and B. S. Williams, "Leaky and bound modes in terahertz metasurfaces made of transmission-line metamaterials," J. Appl. Phys. **113**(3), 1–10 (2013).
35. P. W. C. Hon, A. A. Tavallaee, Q. S. Chen, B. S. Williams, and T. Itoh, "Radiation model for terahertz transmission-line metamaterial quantum-cascade lasers," IEEE Trans. Terahertz Sci. Technol. **2**(3), 323–332 (2012).